RESEARCH ARTICLE

Magnetic graphene oxide for methylene blue removal: adsorption performance and comparison of regeneration methods

Yawei Shi[1] · Haonan Wang[1] · Guobin Song[1] · Yi Zhang[1] · Liya Tong[1] · Ya Sun[1] · Guanghui Ding[1]

Abstract

A series of Fe_3O_4-graphene oxide (GO) composite materials (MGOs) with abundant surface area, rich oxygen-containing functional groups, and magnetic properties were prepared in a facile coprecipitation method and then employed for the adsorptive removal of methylene blue (MB) from water. The kinetic data were better fitted in the pseudo-second-order model than in the pseudo-first-order model, and the intraparticle diffusion model revealed the two-step diffusion process including diffusion in the boundary layer and in the porous structures. The maximum adsorption amounts of MB were calculated to be 37.5–108 mg/g at 25 °C and pH 9 using the Langmuir isotherm model. Thermodynamic study showed that the adsorption process was spontaneous, with $\Delta H°$ of 23.0–49.6 kJ/mol and $\Delta S°$ of 131–249 J•mol^{-1}•K^{-1}. The adsorption amount of MB increased with pH in the range of 4–10. Inorganic ions including Na^+ and Ca^{2+} suppressed the adsorption of MB, and the more pronounced impact of Ca^{2+} was ascribed to its higher valence state. The cetyltrimethylammonium bromide (CTAB) surfactant showed a stronger inhibitory effect than Ca^{2+}. The adsorption mechanism was proposed to be a combination of electrostatic interactions, hydrophobic adsorption, and electron donor–acceptor interactions. Two methods were used for the regeneration of spent MGO, and the results showed that the peroxomonosulfate (PMS) oxidation method was more favorable than the acid washing method, considering the better regeneration ability and lower amount of washing water used. Finally, the reaction mechanism of PMS oxidation was analyzed based on quenching tests and in situ open circuit potential measurements, which proved that OH and $^1O_2$ played dominant roles and that the fine adsorption ability of MGO promoted the reaction between them and MB.

Keywords Magnetic graphene oxide · Adsorption · Methylene blue · Regeneration · Peroxomonosulfate · Advanced oxidation process

Introduction

Dyes with fascinating colors are widely used in human society, but the discharge of dye wastewater may greatly threaten the environment and human health. For example, dyes in wastewater can hinder the growth of plants by suppressing the penetration of sunlight into water (Ceretta et al., 2020). In addition, dyes are known to be related to several severe dysfunctions and diseases, even leading to cancer (Khan

et al., 2020). Methylene blue (MB) is a typical dye that is still widely used in the textile industry (Ighalo et al., 2021). MB is also used in the pharmaceutical industry for the potential treatment of Alzheimer's disease (Schirmer et al., 2011). Through inhalation or ingestion, MB can cause difficulty breathing, methemoglobinemia, mental confusion, and other harm to the human body (Rafatullah et al., 2010). Considering the severe detrimental impacts of MB and other dyes, a variety of remediation methods have been utilized, such as oxidation (Missaoui et al., 2021; Rani and Shanker 2021), membrane separation (Zhao et al., 2021), flocculation/coagulation (Li et al., 2017), and adsorption. Adsorption is a process that occurs due to the affinity of certain adsorbate species to an adsorbent. Compared to other remediation methods, the adsorption process possesses several merits, such as simplicity, easy operation, high efficiency, and the avoidance of unwanted byproducts (Chen et al., 2018; Gupta

✉ Guanghui Ding
guanghuiding@dlmu.edu.cn

[1] College of Environmental Science and Engineering, Dalian Maritime University, Dalian 116026, China

and Khatri 2017; Hajahmadi et al., 2015). Various adsorbents have been applied, including carbon materials (Azari et al., 2020; Partlan et al., 2020; Pirzadeh and Ghoreyshi 2013), metal–organic frameworks (MOFs) (Pirzadeh et al., 2018; Soni et al., 2020), zeolites (Doekhi-Bennani et al., 2021; Ji et al., 2021), and metal oxides (Fatima et al., 2020; Hu et al., 2013). Among these adsorbents, carbon materials stand out due to their tailored structures, well-developed porosity, and ample surface functional groups.

Graphene oxide (GO) is a well-known carbon material that has attracted global attention since its birth. GO has been successfully used for the adsorptive treatment of dye wastewater (Ersan et al., 2017; Khan et al., 2017; Ramesha et al., 2011; Yang et al., 2011). However, the posttreatment separation of GO is difficult due to its good dispersion in water, and residual GO may show some adverse effects on the ecological system (Chen et al., 2012). Recently, magnetic GO (MGO) prepared by compositing GO with magnetic materials has received attention (Doan et al., 2021; Khan et al., 2020; Molaei, 2021; Ramirez-Ubillus et al., 2021; Sadrnia et al., 2021). Due to the magnetic feature of MGO, it can be facilely separated with an external magnetic field after adsorption, which simplifies the water treatment process and avoids the potential unfavorable effects of GO on the water environment.

The magnetic feature of MGO facilitated its recollection after adsorption, but it could not be directly reused after separation due to the occupation of adsorption sites. Thus, the selection of an efficient regeneration method remains an issue (Liu et al., 2020a, b). The thermal regeneration method is a possible choice, but it requires high temperature and thus has a high energy cost. The biological regeneration method is environmentally friendly but generally suffers from a low treatment rate and thus a long operation time (Gamal et al., 2018). The solvent washing method with inorganic (acid, alkali, etc.) or organic solvents (ethanol, acetone, etc.) is also commonly utilized (Lu et al., 2011; Song et al., 2021). However, the use of organic solvents may bring additional organic pollution, while acid or alkali washing may result in large amounts of spent washing water.

Recently, the persulfate-based advanced oxidation process (AOP) has been extensively investigated, where peroxymonosulfate (PMS) and peroxydisulfate (PDS) are used as oxidants (Anfar et al., 2021; Qian et al., 2021). Compared to symmetric PDS, PMS possessing an asymmetric structure is more active and performs better for the mineralization of organic pollutants (Cheng et al., 2021). Magnetic graphene-based materials have been successfully used in AOP for the catalytic degradation of organic pollutants (Gong, 2016; Solís et al., 2021; Wang et al. 2020a, b; Yin et al., 2019). Nevertheless, persulfate-based AOP is generally influenced by water matrix properties, such as inorganic ions and natural organic matter. In addition, the direct application of persulfate-based AOP may adversely impact the water

quality through the release of sulfate anions (Solis et al., 2020). Therefore, using persulfate-based AOP for adsorbent regeneration is considered an attractive approach and has been successfully utilized for the regeneration of activated carbons through thermal activation (Hutson et al., 2012; Wang et al., 2021), ultraviolet activation (An et al., 2015), or electrochemical activation (Liu et al. 2020a, b; McQuillan et al., 2018; Zhou et al., 2020a, 2020b). Considering the catalytic ability of MGO, the spent MGO could act as the catalyst for PMS activation in the regeneration process. Thus, extra energy inputs may be avoided, further improving the convenience and economy of the persulfate-based regeneration method.

In this work, MGO materials were prepared in a facile coprecipitation method and then employed for the adsorptive removal of MB from water. The adsorption performance of MB was studied in detail by investigating the adsorption kinetics, isotherms, and thermodynamics, as well as the effects of pH, inorganic ions, and surfactant. Moreover, the regeneration of MGO was performed by PMS oxidation at ambient temperature and compared with the acid washing method. The reaction mechanism of the catalytic PMS oxidation process is also discussed.

Experimental

Preparation

Magnetic graphene oxide (MGO) was prepared by a coprecipitation method using graphene oxide (GO), $(NH_4)_2Fe(SO_4)_2\cdot6H_2O$, $NH_4Fe(SO_4)_2\cdot12H_2O$, and aqueous ammonia. Appropriate amounts of $(NH_4)_2Fe(SO_4)_2\cdot6H_2O$ and $NH_4Fe(SO_4)_2\cdot12H_2O$ were dissolved in 50 mL water, mixed with 100 mL GO suspension (1 g/L), and then heated at 85 °C in a water bath. Subsequently, under nitrogen protection with mechanical agitation mechanical stirring at 300 r/min, aqueous ammonia was added at a rate of ~ 1 drop per s until the solution pH reached 11. The mixture was stirred for another 1 h and cooled naturally. The precipitate was then magnetically separated, rinsed with water and ethanol, and finally dried to obtain MGO. The feed ratio of Fe(II) and Fe(III) was set as 1:2, and the theoretical mass ratio of GO to Fe_3O_4 was set as 1:2, 1:3, 1:5, or 1:10 to obtain MGO1, MGO2, MGO3, or MGO4. For comparison, plain Fe_3O_4 was prepared in the same manner except that GO was not added. Details for suppliers of the materials are provided in Text S1.1 in the Supplementary Information.

Characterization

The adsorbents were characterized by transmission electron microscopy (TEM), X-ray diffraction (XRD), Fourier

transform infrared (FTIR), nitrogen sorption, vibrating sample magnetometry (VSM), zeta potential measurements, X-ray photoelectron spectroscopy (XPS), and open circuit potential (OCP). The characterization details are provided in Text S1.2 in the Supplementary Information.

Adsorption and oxidation experiments

Adsorption tests were performed in batch mode using a shaker bath with a rotation speed of 150 rpm, and the concentrations of methylene blue (MB), sulfamethoxazole (SMX), and bisphenol A (BPA) in the solution after adsorption were measured with a TU-1901 UV–vis spectrometer at 664, 276, and 260 nm, respectively. NaOH or HCl was added when needed to investigate the effect of pH value. NaCl, $CaCl_2$, or cetyltrimethylammonium bromide (CTAB) was added when needed.

Kinetic studies were performed by fitting pseudo-first-order (PFO), pseudo-second-order (PSO), and intraparticle diffusion models. The isotherm data were fitted to the Langmuir and Freundlich models. For thermodynamic studies, the standard Gibbs free energy change ($\Delta G°$) and the standard enthalpy and entropy change ($\Delta H°$ and $\Delta S°$) were calculated.

Regeneration of the adsorbent was conducted using two methods. For the acid washing method, the spent adsorbent after adsorption of MB in 50 mL of 50-mg/L solution was magnetically separated, washed with 0.1 M HCl and water three times, and then used for the next adsorption run. For the peroxomonosulfate (PMS) oxidation method, the magnetically separated spent adsorbent was treated with 50 mL of 4-mM PMS for 4 h, washed with 50 mL of water to remove residual PMS, and then used for the next run.

To illustrate the PMS oxidation mechanism, additional catalytic oxidation experiments were conducted. Certain amounts of MGO, PMS, and MB solution were added to a glass flask and mechanically stirred in a water bath at 25 °C. For comparison, an adsorption control test was conducted without the addition of PMS, and the initial pH was tailored to 3.2 which was the value in the presence of PMS. Quenchers including methanol, tert-butanol (TBA), furfuryl alcohol (FFA), and benzoquinone (BQ) were added when needed. The apparent rate constants (k_{obs}) were obtained from the linear form pseudo-first-order kinetic model. More details concerning the data analysis in the adsorption and oxidation experiments are provided in Text S1.3 in the Supplementary Information.

Results and discussion

Characterization of the adsorbents

TEM measurements were employed to investigate the morphology of graphene oxide (GO) and magnetic graphene oxide 1 (MGO1). GO possessed a typical sheet-like morphology with wrinkles (Fig. 1a), and the transparent nature of the sheet indicated the exfoliation of GO to monolayer or few-layer structures. In addition to the GO sheet, additional aggregates of spherical particles were observed in the image of MGO1 (Fig. 1b), which were introduced in the coprecipitation process. XRD patterns of GO, Fe_3O_4 MGO1, and MGO1-MB (the sample after MB adsorption) are displayed in Fig. 1c. The characteristic peak at $2\theta = 11.0°$ was revealed in the pattern of GO, which was obviously shifted to a lower diffraction angle compared to the diffraction angle of graphite at $2\theta = 26.4°$ (JCPDS 41–1487), attributed to the increased graphite layer spacing upon the introduction of oxygen-containing functional groups. In the pattern of MGO1, the peak ascribed to GO was slightly shifted to $2\theta = 10.7°$, suggesting the insertion of iron oxide particles between the GO layers. In addition, the peak was dramatically weakened compared to GO. On the one hand, ultrasound treatment and the introduction of iron oxide particles may interrupt the staking of GO layers (Yang et al., 2012), leading to decreased diffraction intensity. On the other hand, partial reduction of GO may occur considering the alkaline environment in the coprecipitation process (Cheng et al., 2012; Zhu et al., 2017), which may also weaken the diffraction peak. Moreover, the additional peaks observed in the pattern of MGO1 were ascribed to Fe_3O_4 (JCPDS 19–0629), suggesting the successful preparation of the magnetic composite material. The XRD pattern of MGO1-MB was similar to the XRD pattern of MGO1, indicating the stability of the adsorbent during the adsorption process.

Nitrogen sorption isotherms were measured to investigate the porosities of the materials (Fig. 1d), and the calculated textural properties are provided in Table 1. The low specific surface area (S_{BET}) of GO was similar to the results in previous reports (Lee et al., 2019; Zhu et al., 2020), which was ascribed to the agglomeration of GO sheets in the powder sample. Interestingly, the S_{BET} of MGO1 was found to be larger than the S_{BET} of GO and Fe_3O_4. During the coprecipitation process, aqueous ammonia was added for the precipitation of iron species, creating an alkaline environment. Generally, an alkaline environment would lead to the reduction of GO. For example, GO was reduced with ammonia solution at 90 °C to produce reduced GO (rGO) (Zhu et al., 2017). In another work, rGO was obtained by reduction of GO with urea at 95 °C (Cheng et al., 2012). In addition, the reduction of GO could lead to an increased surface area (Yang et al., 2012). Thus, we inferred that the increased surface area here was attributed to the partial reduction of GO, which was also reflected by the textural properties of the samples with higher Fe_3O_4 amounts (MGO2-4) (Fig. S1 and Table S1). As shown in Table S1, the surface areas of MGO2-4 were all higher than the surface area of GO but lower than the surface area of MGO1, which was attributed
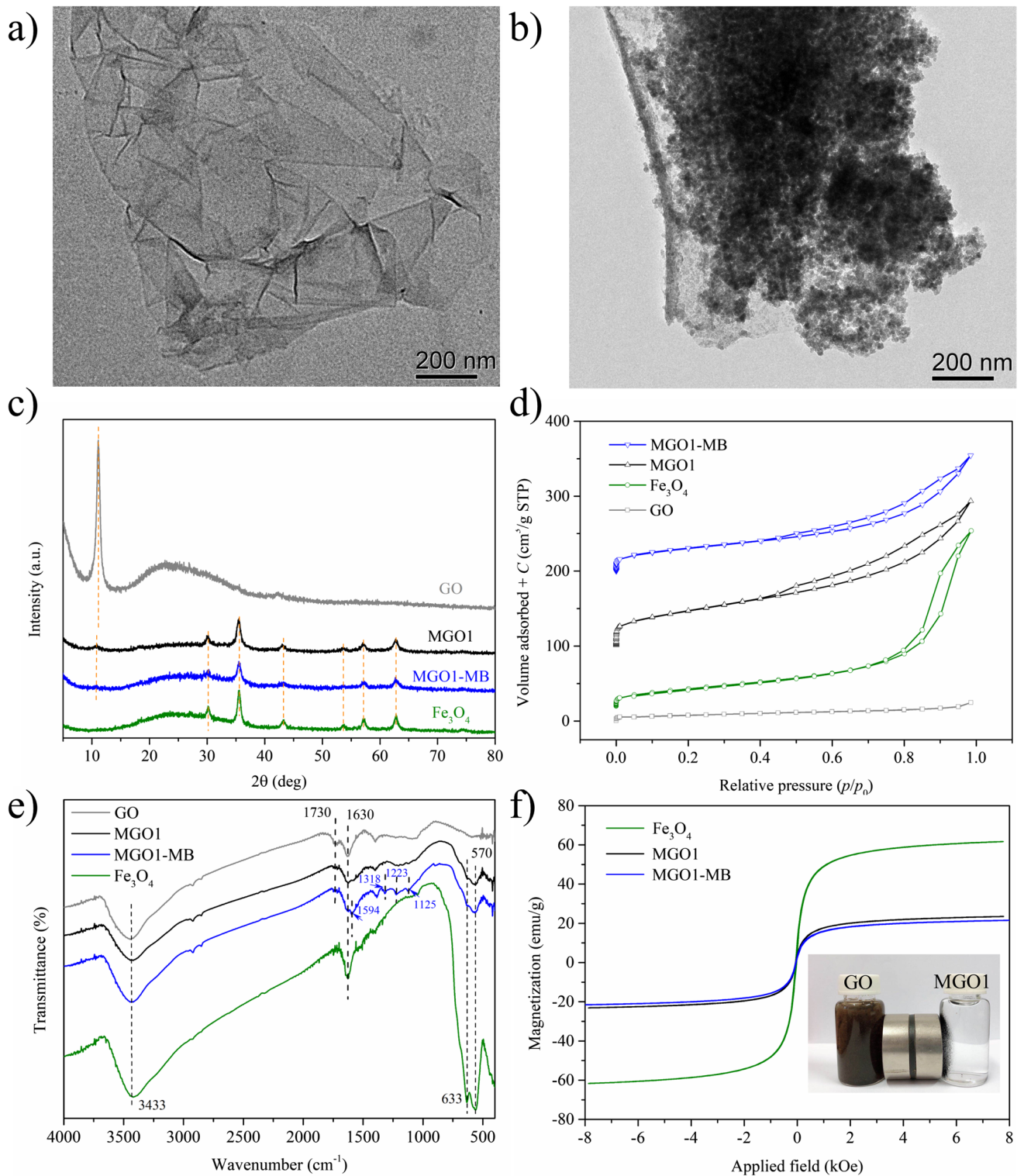
Fig. 1 TEM image of GO (**a**) and MGO1 (**b**), XRD patterns (**c**), nitrogen sorption isotherms (**d**), FTIR spectra (**e**), and magnetization curves (**f**) of the samples

to the lower amounts of GO in these samples and thus weaker enhancement of the surface areas in the coprecipitation process. The reduction degree in this work was limited

considering the relatively weaker conditions compared to the previous work (Zhu et al., 2017), evidenced from the XRD analysis where the characteristic peak of GO still existed in

Table 1 Textural properties of the adsorbents

Sample	S_{BET} (m²/g)	V_{total} (cm³/g)	V_{micro} (cm³/g)	D_p (nm)
GO	28.5	0.0379	0.00341	5.32
Fe₃O₄	88.2	0.362	0.000	16.4
MGO1	173	0.299	0.0243	6.91
MGO1-MB	112	0.239	0.0126	8.54

the composite material (Fig. 1c), which was different from the case reported previously where the corresponding peak could no longer be observed after reduction (Zhu et al., 2017). The decreased surface area after MB adsorption was ascribed to the occupation of the MGO1 surface by MB molecules.

FTIR spectra of the samples are illustrated in Fig. 1e. Broad bands at approximately 3433 and 1630 cm^{-1} were observed in all the samples attributed to the stretching and bending vibrations of -OH groups (Chen et al., 2017; Zhang et al., 2019). The peak at 1730 cm^{-1} observed in the patterns of GO was ascribed to the stretching vibration of C=O groups (Muniyalakshmi et al., 2020), while the two peaks at 663 and 570 cm^{-1} in the pattern of Fe₃O₄ were attributed to Fe–O bonds (Deng et al., 2019). These three peaks were observed in the pattern of MGO1 with reduced intensities, indicating the successful preparation of the composite material. After the adsorption of MB, additional bands at 1594, 1318, 1223, and 1125 cm^{-1} were observed and attributed to the C–N stretching vibration of the heterocycle, C–N stretching vibration of the terminal dimethylamino group, and C–C stretching and bending vibrations of the heterocycle respectively (Ovchinnikov et al., 2016), verifying the adsorption of MB on the adsorbent. The magnetization curves of the adsorbents are compared in Fig. 1f. As expected, the saturation magnetization of MGO1 was lower than the saturation magnetization of Fe₃O₄ alone. After the adsorption of MB, the saturation magnetization dropped slightly. When dispersed in water at the same dosage, MGO1 could be effectively separated with an external magnetic field while GO could not (Fig. 1f inset), verifying the excellent magnetic separation property of the composite adsorbent.

XPS measurements were performed to further investigate the chemical compositions of the adsorbents (Fig. 2 and Table 2). The survey scans proved the presence of C1s, O1s, and Fe2p peaks in MGO (Fig. 2a), consistent with the FTIR results. The ratio of Fe to C increased from MGO1 to MGO4 (Table 2). Moreover, based on deconvolution of the Fe2p spectra (Fig. S2), both Fe(II) and Fe(III) were revealed and the ratios of Fe(III) to Fe(II) were found to be close to 2 (Table 3), supporting the XRD results.

Furthermore, the ratio of O to C in the carbon structure was calculated, where the oxygen content in MGO was obtained by subtracting the oxygen atoms in Fe₃O₄.

Compared in Table 2, the ratios of (O-4/3Fe)/C in the MGO samples (0.286–0.329) were all considerably smaller than the ratios in GO (0.471), which was assigned to the reduction of GO in the coprecipitation process. In addition, deconvolution of the C1s spectra led to three peaks at approximately 284.8, 286.6, and 288.7 eV, which were attributed to C–C/C=C, C–O, and C=O species respectively (Huang et al., 2017; Wang et al., 2019). The relative content of C–C/C=C was higher for MGO (54.4–60.1%) than GO (43.8%) (Fig. 2b–f and Table 3), further verifying the reduction of GO.

Effect of pH

The adsorbents were employed for the adsorption of methylene blue (MB) at a series of pH values. As displayed in Fig. 3a, the adsorption amounts of MB were generally elevated with an increase in pH, indicating that an alkali environment was more favorable for MB adsorption. Considering the cationic nature of MB, we inferred that electrostatic interactions between MB and the adsorbent surface were involved in the adsorption process (Eltaweil et al., 2020; Song et al., 2021).

According to zeta potential measurements, the surface of MGO1 was positively charged at a lower pH value but negatively charged at a higher pH value (Table 4). Thus, electrostatic repulsion between MB cations and the adsorbent surface was expected at a lower pH. The relatively higher concentration of H$^+$ ions may also lead to stronger competition with MB for the adsorption sites (Yao et al., 2021). These reasons resulted in the lower adsorption amounts of MB in the acidic environment. As discussed in the "Characterization of the adsorbents" section, abundant functional groups including -OH and -COOH were present on the adsorbent surface. The pK$_a$ values of benzoic acid and phenol with different substituents were in the range of 3.43–4.37 (Hollingsworth et al., 2002) and 7.15–10.30 (Gross and Seybold 2001), respectively. Thus, deprotonation of -COOH occurs at approximately pH 4, and deprotonation of -OH occurs at a higher pH. With an increase in the solution pH, the adsorbent surface became negatively charged due to the gradual deprotonation of these groups, leading to electrostatic attraction towards MB and thus higher adsorption amounts.

Electrostatic interactions were not the only adsorption mechanism, because MB could still be adsorbed at pH 4 when the adsorbent surface was positively charged (Table 4), and electrostatic repulsion was expected. Based on the results here and previous works (E et al. 2020; He et al., 2020; Kah et al., 2017), other mechanisms including hydrophobic adsorption and electron donor–acceptor (EDA) interactions also played a role, which was also evidenced
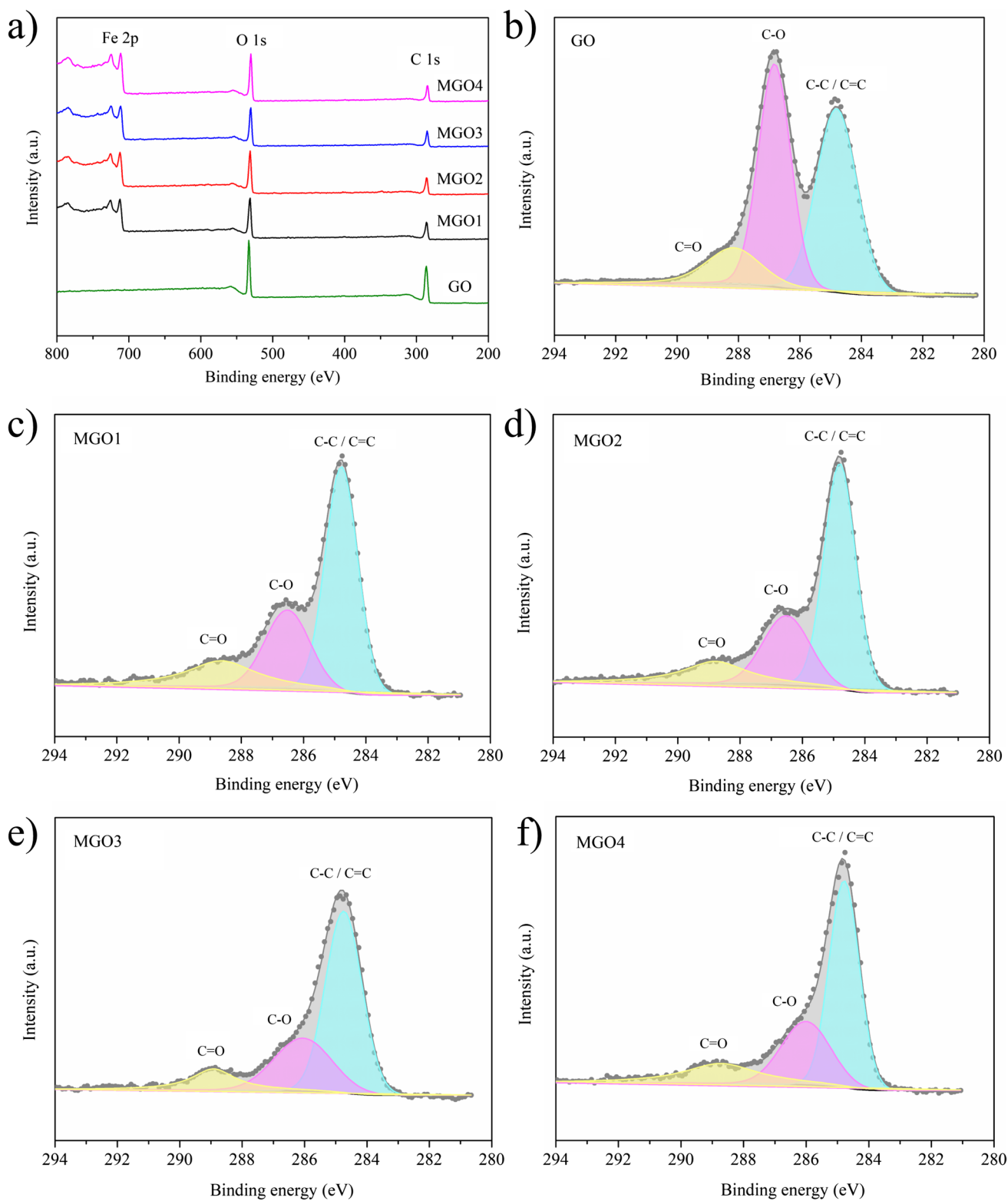
Fig. 2 XPS survey scan of GO and MGO (**a**) and the XPS C1s spectra of GO (**b**) and MGO1-4 (**c**–**f**)

Table 2 XPS analysis of the adsorbents

Sample	C (atom. %)	O (atom. %)	Fe (atom. %)	Fe/C	(O-4/3Fe)/C
MGO1	44.7	37.9	17.4	0.389	0.329
MGO2	41.7	39.1	19.2	0.460	0.324
MGO3	41.8	38.6	19.6	0.469	0.298
MGO4	38.2	40.0	21.8	0.571	0.286
GO	68.0	32.0	—	—	0.471

by the adsorption results with GO and the values of $\Delta H°$ discussed below.

For comparison, MB adsorption with GO was also investigated. A similar increasing trend of adsorption amount with increasing pH was revealed (Fig. S3a), which was also attributed mainly to the change in the surface charge of GO (Table 4). Moreover, the adsorption of MB with GO was conducted at $C_0 = 150$ mg/L, higher than the value of 50 mg/L with the magnetic adsorbents. Actually, almost complete removal of MB was achieved when employing GO for the treatment of 50 mg/L MB. The surface of GO was negatively charged in the whole pH range of 4–10, suggesting stronger electrostatic attraction with MB. In addition, the better removal of MB with GO was ascribed to its aromatic structure, which could interact with MB efficiently through EDA interactions in the form of π-π stacking. The magnetic adsorbents contained lower amounts of GO, and Fe_3O_4 lacked an aromatic structure, leading to weaker EDA interactions. Consequently, the adsorption amounts followed the order of GO > MGO1 > MGO2 > MGO3 > MGO4 > Fe$_3$O$_4$. Although the magnetic adsorbents possessed lower adsorption amounts, they could be facilely separated due to the magnetic feature and were considered more favorable for potential applications.

Kinetic, isotherm, and thermodynamic studies

As observed above, an alkali environment was more favorable for MB adsorption. According to the local standard of GB 18,918–2002 in China, the pH of wastewater should be in the range of 6–9. Thus, we employed a pH of 9 instead of 10 as the optimum pH condition in the following studies because a pH of 10 was not feasible from an industrial viewpoint. As shown in Fig. 3b and Fig. S3b, the kinetic data were better fitted in the PSO model than in the PFO as indicated by the larger R^2 and closer calculated q_e values (Table 5). Recently, it was demonstrated that the adsorption mechanism could not be proposed directly based on the better fitting result in PSO than PFO (Hubbe, 2021; Tran et al., 2017). Instead, this reaction stems from a mathematical basis (Mahdavi et al., 2018; Simonin, 2016; Tan and Hameed 2017). Considering this factor, the data were further analyzed with the intraparticle diffusion model. The curves consisted of two linear stages (Fig. 3c and Fig. S3c), indicating the two-step diffusion process with diffusion in the boundary layer and in the porous structures (Tan and Hameed 2017), and the declining rate constants ($k_1 > k_2$, Table 6) suggested that adsorption equilibrium was gradually reached on the surface of MGO and GO. As shown in Table 1, the micropore volumes of the samples are very low, and the molecular size of MB, which is 1.42 nm×0.62 nm×0.16 nm (Zhang et al., 2006), is much smaller than the average pore sizes of the adsorbents, indicating that the diffusion of MB in the porous structure is favorable also reflected from the fitting results in the intraparticle diffusion model where relatively low slopes of the second stage are observed (Fig. 3c). Once the MB molecule passed through the boundary layer and entered the porous network, its diffusion was fast and adsorption equilibrium was established in a short time.

Isotherm studies were performed by conducting MB adsorption under a series of initial concentrations. As depicted in Fig. 3d and Fig. S3d, q_e first increased with C_e and then approached stability, suggesting the gradual saturation of adsorption sites. Fitting results in the Langmuir and Freundlich models (Table 7) showed that the adsorption process could be adequately described by both models (Hubbe, 2021). The maximum adsorption amount (q_{max}) dropped from MGO1 to MGO4 (Table 7), in line with the order in the "Effect of pH" section. The Freundlich constant (K_F), which represented the adsorption amount, followed a consistent order, further verifying the reliability of the results.

Table 3 XPS deconvolution results for C1s and Fe2p of the adsorbents

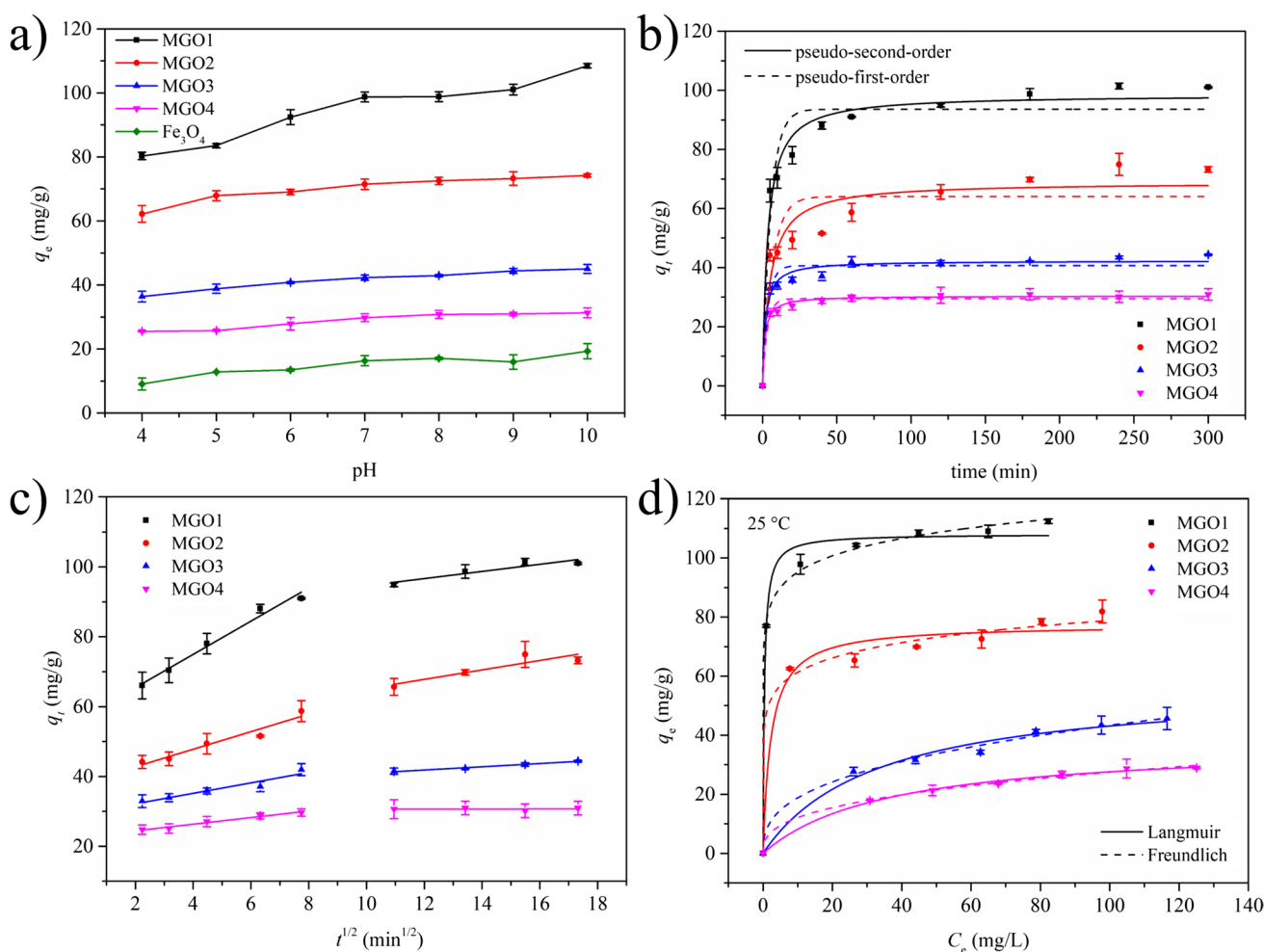| Samples	C 1 s			Fe 2p		
	C–C/C=C (%)	C–O (%)	C=O (%)	Fe(II) (%)	Fe(III) (%)	Fe(III)/Fe(II) (%)
MGO1	54.7	25.8	19.5	34.8	65.2	1.87
MGO2	57.8	25.9	16.3	33.8	66.2	1.96
MGO3	60.1	27.6	12.3	33.3	66.7	2.00
MGO4	54.4	27.1	18.5	33.1	66.9	2.02
GO	43.8	43.1	13.1	—	—	—

Fig. 3 Effect of pH on adsorption amount of MB with the magnetic adsorbents (**a**), fitting in pseudo-first-order and pseudo-second-order models (**b**), fitting in the intraparticle diffusion model (**c**), and adsorption isotherms of MB (**d**) (Experimental conditions: $C_0 = 100$ mg/L for a–c; adsorbent dosage $= 0.5$ g/L for a–d; pH $= 9$ for b–d; temperature $= 25$ °C for a–d)

Table 4 Zeta potentials of the adsorbents at different pH values

pH	4	7	10
MGO1	6.6 ± 0.3	-8.5 ± 0.2	-35.7 ± 1.1
GO	-39.0 ± 0.8	-39.1 ± 0.4	-43.1 ± 1.0
Fe$_3$O$_4$	18.4 ± 0.2	-8.4 ± 2.3	-21.5 ± 0.2

The performance of MGO1 for MB adsorption was compared with previous studies. As shown in Table S2, q_{max} of MB on MGO1 was comparable with various adsorbents including MOF, zeolite, and carbon materials. Although some of the adsorbents showed larger adsorption amounts than MGO1, they could not be magnetically

Table 5 PFO and PSO kinetic models for MB adsorption on the adsorbents

Adsorbents	Exp. q_e (mg/g)	PFO model			PSO model		
		Cal. q_e (mg/g)	k_1 (10^{-2} min^{-1})	R^2	Cal. q_e (mg/g)	k_2 (10^{-3} g/(mg·min))	R^2
MGO1	101	93.6	3.62	0.930	98.5	0.545	0.980
MGO2	73.2	64.0	4.81	0.823	68.9	1.04	0.912
MGO3	44.4	40.6	6.28	0.938	42.3	3.03	0.974
MGO4	30.9	29.5	5.78	0.966	30.4	3.99	0.990
GO	479	404	17.3	0.831	433	0.548	0.911

Table 6 The intraparticle diffusion constants for MB adsorption on the adsorbents

Adsorbents	k_1 (mg•g^{-1} min$^{-0.5}$)	C_1 (mg/g)	R_1^2	k_2 (mg•g^{-1} min$^{-0.5}$)	C_2 (mg/g)	R_2^2
MGO1	4.76	55.9	0.980	1.02	84.4	0.872
MGO2	2.52	37.7	0.943	1.35	51.6	0.812
MGO3	1.50	29.2	0.796	0.465	36.3	0.980
MGO4	0.945	22.5	0.945	4.81e-3	30.6	0.001
GO	14.0	254	0.966	12.0	276	0.962

Table 7 Isotherm models for MB adsorption on the adsorbents

T (°C)	Adsorbent	Langmuir model			Freundlich model		
		q_{max} (mg/g)	K_L (L/mg)	R^2	K_F ((mg/g) (L/mg)$^{1/n}$)	n	R^2
20	MGO1	103	0.780	0.997	69.2	10.7	0.992
	MGO2	71.7	0.416	0.990	46.9	10.8	0.998
	MGO3	47.4	0.0364	0.995	8.57	3.13	0.999
	MGO4	34.6	0.0204	0.960	3.33	2.38	0.977
	GO	494	1.10	0.987	371	15.5	0.985
25	MGO1	108	2.52	0.991	78.9	12.3	0.998
	MGO2	77.4	0.443	0.972	47.7	9.15	0.990
	MGO3	57.3	0.0305	0.984	8.17	2.76	0.992
	MGO4	37.5	0.0279	0.996	5.34	2.81	0.996
	GO	519	1.69	0.991	389	14.5	0.994
30	MGO1	122	1.95	0.992	84.4	10.2	0.992
	MGO2	82.8	0.709	0.988	57.7	12.1	0.997
	MGO3	59.9	0.0454	0.934	11.6	3.15	0.963
	MGO4	36.3	0.0402	0.998	7.84	3.52	0.996
	GO	541	1.97	0.977	393	12.6	0.994
35	MGO1	131	2.12	0.986	88.8	9.35	0.989
	MGO2	85.1	0.871	0.988	61.3	13.0	0.997
	MGO3	60.4	0.0598	0.960	15.3	3.71	0.981
	MGO4	42.3	0.0326	0.996	6.98	3.00	0.999
	GO	574	36.3	0.986	488	22.6	0.985

separated due to the lack of magnetic species. Thus, MGO1 can be considered a promising candidate for MB adsorption with both a large adsorption amount and magnetic properties.

The temperature effect on MB adsorption was studied as well. With an increase in adsorption temperature, q_{max} of MB was elevated on all the adsorbents (Fig. S3d for GO, Fig. 3d and Fig. S4a-c for MGO, Table 7), suggesting the endothermic properties of the adsorption process. Furthermore, thermodynamic parameters including $\Delta G°$, $\Delta H°$, and $\Delta S°$ were calculated by fitting the van't Hoff equation (Fig. S4d and Table 8). The negative $\Delta G°$ values suggested that the adsorption of MB on MGO and GO was spontaneous. The absolute value of $\Delta G°$ declined in the order of MGO1 > MGO2 > MGO3 > MGO4, again proving that MGO1 was more favorable for MB adsorption. The positive $\Delta H°$ value implied endothermic properties, in accordance with the increased q_{max} at a higher temperature.

The $\Delta H°$ value for physical or chemical adsorption was reported to be < 20 and 80–200 kJ/mol respectively (Li et al., 2010). For MGO, the absolute values of $\Delta H°$ were in the range of 23.0–49.6 kJ/mol, which indicated the combination of physical and chemical adsorption in the process. As reported previously, the energy associated with nonspecific hydrophobic, electrostatic, or EDA interactions was approximately 0.4–4, > 20, or 4–167 kJ/mol, respectively (Kah et al., 2017). These types of interactions may be involved, and electrostatic and EDA interactions may play a larger role in the adsorption process. Here, this conclusion does not conflict with the result observed in the kinetic studies when the intraparticle diffusion model was used because MB molecules had to pass through the boundary layer and then interact with the adsorbent surface through these interactions. The $\Delta S°$ value is known to be related to the change in disorder. When aqueous dye molecules were adsorbed on the solid MGO or GO surface, they became bound and suffered

Table 8 Adsorption thermodynamics for MB adsorption on the adsorbents

Adsorbent	T (°C)	$\ln K_c$	$\Delta G°$ (kJ/mol)	$\Delta H°$ (kJ/mol)	$\Delta S°$ (J•mol^{-1}•K^{-1})
MGO1	20	9.52	−23.2	49.6	249
	25	10.1	−25.1		
	30	10.3	−26.0		
	35	10.6	−27.0		
MGO2	20	8.51	−20.7	31.1	177
	25	8.70	−21.6		
	30	8.98	−22.6		
	35	9.11	−23.3		
MGO3	20	6.98	−17.0	29.3	158
	25	7.09	−17.6		
	30	7.39	−18.6		
	35	7.53	−19.3		
MGO4	20	6.30	−15.4	23.0	131
	25	6.57	−16.3		
	30	6.63	−16.7		
	35	6.79	−17.4		
GO	20	11.1	−27.0	65.8	316
	25	11.4	−28.2		
	30	11.5	−29.1		
	35	12.5	−32.0		

loss of freedom, leading to decreased disorder. However, desorption of water molecules (Teli and Nadathur 2018) and changes in the adsorbent surface (Dai et al., 2018) occurred at the same time, which may lead to increased entropy. Here, the positive $\Delta S°$ value reflected the net increase in disorder in the whole process.

Generally, hydrophobic adsorption and electron donor–acceptor interactions were also involved in the adsorption process of some emerging pollutants, especially the pollutants with aromatic structures. Thus, the adsorption of two typical emerging pollutants, sulfamethoxazole

(SMX), and bisphenol A (BPA) was further investigated. As illustrated in Fig. S5 and Table S3, the q_{max} values of SMX and BPA were 25.0 and 33.8 mg/g respectively, indicating that MGO could also be used as a potential candidate for the treatment of these pollutants. The relatively lower adsorption amounts for SMX and BPA compared to MB were attributed to the absence of electrostatic attraction in the adsorption process of these two pollutants.

Effect of inorganic ions and surfactant

The inorganic ions and surfactants present in wastewater may impact the adsorption of dyes. To illustrate this issue, NaCl and CaCl$_2$, typical inorganic salts, and CTAB, a widely used cationic surfactant, were added to synthetic wastewater. As displayed in Fig. 4a, q_e dropped in the presence of NaCl, CaCl$_2$, and CTAB. These added cationic species (Na$^+$, Ca^{2+}, and CAT$^+$) could screen the negatively charged surface sites, which was detrimental for the adsorption of MB through electrostatic attraction (Singh et al., 2019). Compared to Na$^+$, the more pronounced impact of Ca^{2+} (Fig. 4a) was ascribed to its higher valence state. However, CTA$^+$, as a monovalent cation showed a stronger inhibitory effect than Ca^{2+}, even though it was added in a much smaller amount (Fig. 4a), suggesting that the adsorption of bulky CTA$^+$ cations (C$_{19}$H$_{42}$N$^+$) led to the occupation of more surface space than in the case of inorganic ions; thus, not only electrostatic attraction but also EDA interaction and hydrophobic adsorption of MB were hindered. As a result, q_e of MB dropped to a greater extent.

Reusability for MB adsorption

The commonly employed acid washing method was first used for the regeneration of MGO because it possessed relatively weaker adsorption abilities towards MB at lower pH values. During acid washing, the color of the solution turned from transparent to blue, indicating desorption of MB
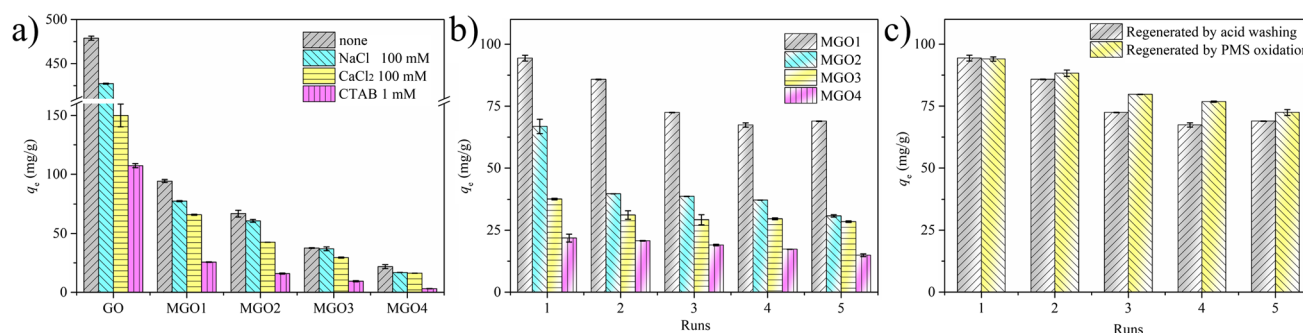

Fig. 4 Effects of inorganic ions and CTAB on MB adsorption (**a**), reusability of MGO1-4 by acid washing (**b**), and a comparison of the reusability of MGO1 by acid washing and PMS oxidation (**c**) (experimental conditions: C_0 = 50 mg/L for MGO1-4 and 150 mg/L for GO; adsorbent dosage = 0.5 g/L; temperature = 25 °C)

from the spent adsorbent. After acid washing three times, the regenerated MGO was used for the next adsorption run. As shown in Fig. 4b, q_e of MB decreased gradually in the five consecutive adsorption runs. The decreased amount of adsorption was attributed to residual MB on the surface of MGO. As discussed in the "Effect of pH" section, although electrostatic repulsion existed between MB and the MGO surface at lower pH values, hydrophobic adsorption, and electron donor–acceptor (EDA) interaction could still lead to the adsorption of MB. In other words, the adsorbed MB could not completely desorb in the regeneration process. In addition, although repeated washing could enhance the desorption of MB, more spent washing water would be produced, which needs further treatment. Thus, the acid washing method was not favorable from a practical viewpoint.

Furthermore, taking MGO1 as an example, PMS oxidation was employed as an alternative adsorbent regeneration method. During the PMS oxidation process, we observed that the color of the solution turned light blue first, and the solution pH was measured to be approximately 2.7. We inferred that this acidic environment led to the desorption of MB. However, the pH value of 2.7 was much higher than the pH in the acid washing process where 0.1 M HCl was employed. Thus, desorption only partially contributed to the PMS oxidation process. In addition, the light blue color remained for a while and then gradually faded, which was different from the case in acid washing where the blue color remained. In this case, the residual MB in the solid phase should be limited from the viewpoint of adsorption equilibrium, suggesting that the oxidation of MB favored the regeneration of surface sites. As shown in Fig. 4c, the PMS oxidation method was more effective for the regeneration of MGO1 than the acid washing method. The decreased q_e of MB in the consecutive adsorption runs was attributed to the degradation products of MB, which occupied some sites on the surface of MGO1 and hindered the adsorption of MB.

Reaction mechanism of the PMS oxidation method

A reusability test showed that PMS oxidation could efficiently regenerate the magnetic adsorbent, but the reaction mechanism of the catalytic oxidation process remained unclear. Thus, additional experiments were conducted to illustrate the reaction mechanism. Magnetic adsorbents (MGO1-4) were first employed for catalytic oxidation of MB in the presence of PMS (Fig. 5a), and the apparent rate constants (k_{obs}) were calculated (Fig. S6a). The removal efficiency of MB in the catalytic oxidation system followed the order of MGO1 > MGO2 > MGO3 > MGO4, which was in accordance with the order of adsorption amounts obtained in the "Effect of pH" section. Furthermore, a fine linear trend ($R^2 = 0.972$) between k_{obs} and q_e was observed (Fig. 5b), indicating that a stronger adsorption ability led

to faster oxidative removal of MB. Generally, two types of reaction mechanisms are involved in the PMS oxidation process, i.e., the reactive oxidative species (ROS) pathway and the nonradical electron-transfer pathway (Zhou et al., 2020a, 2020b). Hydroxyl radicals (OH), sulfate radicals (SO_4^-), superoxide radicals (O_2^-), and singlet oxygen ($^1O_2$) are typical ROS involved in the PMS-based oxidation process; thus, the effects of quenchers (methanol, TBA, BQ, and FFA) on MB removal were studied. As depicted in Fig. 5c, the addition of quenchers reduced MB removal, but the removal values in the presence of quenchers still exceeded the adsorption control, suggesting the involvement of more than one ROS in the reaction process. The k_{obs} values were further calculated (Fig. S6b and Fig. 5c inset) and analyzed. Methanol is considered an efficient quencher for both OH and SO_4^-, while TBA is known to effectively quench OH rather than SO_4^-. Thus, k_{obs} values similar to the k_{obs} values of methanol and TBA (Fig. 5c inset) suggested the negligible contribution of SO_4^- to MB removal. The relative contributions of OH and adsorption were calculated to be 33.2% and 17.7% by comparing the corresponding k_{obs} values to that of the reaction control.

BQ and FFA as quenchers of O_2^- (Yang et al., 2021) and $^1O_2$ (Guo et al., 2021) respectively, could suppress the reaction as well (Fig. 5c). When simply comparing the k_{obs} values, the contributions of O_2^- and $^1O_2$ were calculated to be 44.0% and 46.8%, respectively. However, adding up the contributions of OH, O_2^-, $^1O_2$, and adsorption resulted in an unreasonable value of 141.7%. The standard redox potential of O_2^- was –0.34 V, much lower than the standard redox potential of OH (1.8–2.7 V) and $^1O_2$ (2.2 V) (Khan et al., 2021); thus, O_2^- possessed weak reactivity (Zhang et al., 2021). Based on the results here and previous work (Tian et al., 2020; Wang et al., 2020a, 2020b), we inferred that O_2^- did not directly participate in the reaction, but worked as a precursor that transferred into $^1O_2$ through recombination and reaction with water. The addition of BQ quenched O_2^- and hindered its transformation into $^1O_2$; thus, the removal of MB was evidently reduced. In the presence of FFA, MB removal efficiency was suppressed to a larger degree, which was ascribed to the ability of $^1O_2$ to be produced in other routes, such as the self-decomposition of PMS (Tian et al., 2020). Excluding O_2^-, the sum of relative contributions including OH, $^1O_2$, and adsorption was 97.7%, which was close to 100% and reasonable. The nonradical electron-transfer pathway was demonstrated to play a determining role in some PMS-based catalytic systems (Fan et al., 2021; Shi et al., 2020). In situ OCP measurements have been successfully employed previously to characterize the electron-transfer pathway, where the potential of the catalyst was raised upon PMS addition into the solution, indicating the formation of a metastable catalyst-PMS* complex (Ren et al., 2020). However, in this work, although the initial potential of the MGO1 catalyst was slightly increased compared to bare
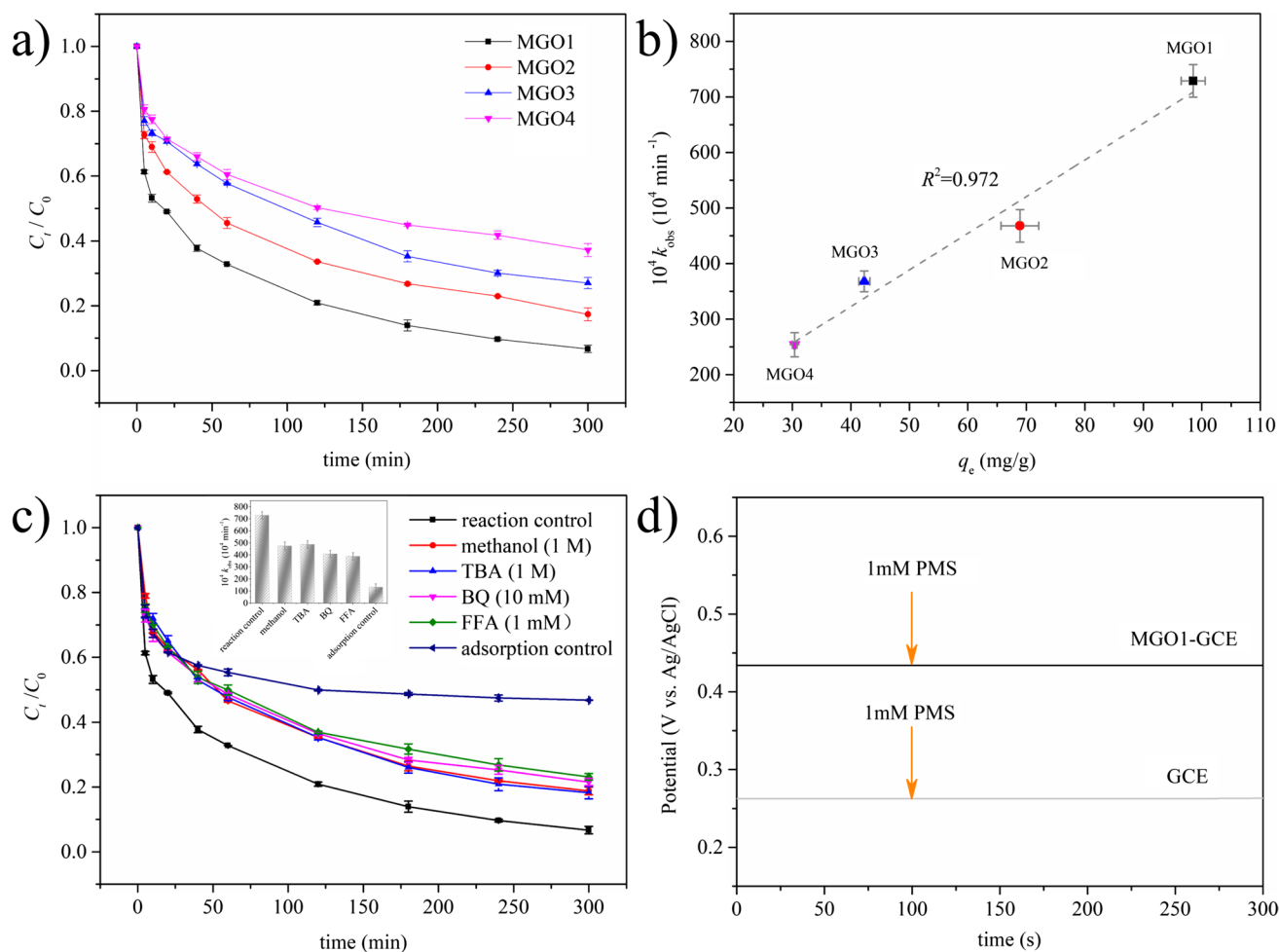
Fig. 5 Removal of MB in the PMS/MGO system (**a**), linear correlation between k_{obs} and q_e (**b**), effect of quenchers in the PMS/MGO1 system (**c**), and the open circuit potential-time curves on MGO1-GCE and GCE (**d**) (experimental conditions: $C_0 = 50$ mg/L; adsorbent dosage = 0.5 g/L; PMS = 1 mM; temperature = 25 °C)

GCE, the addition of PMS did not trigger an obvious change in its potential (Fig. 5d), disproving the involvement of the non-radical electron-transfer pathway in the MGO1/PMS system. Based on the above discussion, OH and $^1O_2$ as ROS played dominant roles in the reaction process. Considering the short lifetime of these reactive species, they existed mainly in the boundary layer between the solution and the surface of the MGO1 catalyst. Thus, adsorption also played an important role, which helped to bring MB to the catalyst surface and promote the reaction between ROS and MB.

Conclusions

A series of Fe_3O_4-graphene oxide (GO) composite materials with increasing Fe_3O_4 loading amounts was synthesized in a facile coprecipitation method and characterized by TEM, XRD, nitrogen sorption, FTIR, zeta potential measurements, VSM, and XPS. The characterization results showed that GO was partially reduced during the preparation process, and the resulting composite material possessed abundant surface area, rich oxygen-containing functional groups, and magnetic properties. The materials were then employed for the adsorptive removal of methylene blue (MB) from water. The alkali environment was more favorable for MB adsorption, which was attributed to the enhanced electrostatic attraction between MB cations and the negatively charged surface groups at a higher pH. In addition, other mechanisms including hydrophobic adsorption and electron donor–acceptor (EDA) interactions, also played a role. A kinetic study showed that the PSO model could better describe the adsorption process than the PFO model. Further analysis based on the intraparticle diffusion model revealed the two-step diffusion process including diffusion in the boundary layer and in the porous structures. Isotherm studies showed that both the Langmuir and Freundlich models

could adequately describe the adsorption process, and the maximum adsorption amounts of MB were calculated to be 108, 77.4, 57.3, and 37.5 mg/g for MGO1-4 (magnetic graphene oxide 1–4). Although these values were lower than the value of GO (519 mg/g), they could be facilely separated due to the magnetic feature, which was more favorable for potential applications. Thermodynamic studies showed that the adsorption processes on MGO1-4 were spontaneous, with $\Delta H°$ of 49.6–23.0 kJ/mol and $\Delta S°$ of 249–131 J•mol^{-1}•K^{-1}. Na$^+$, Ca^{2+}, and CAT$^+$ suppressed the adsorption of MB in the order of Na$^+$ < Ca^{2+} < CAT$^+$, and the stronger inhibition effect of CTA$^+$ was attributed mainly to its bulky structure. The reusability test showed that the PMS oxidation method was more favorable than the acid washing method, considering the better regeneration ability and lower amount of washing water used in the former case. Finally, the reaction mechanism of PMS oxidation was analyzed based on quenching tests and in situ OCP measurements, which proved that OH and $^1O_2$ played dominant roles and that the fine adsorption ability of MGO promoted the reaction between them and MB.

Supplementary Information The online version contains supplementary material available at https://doi.org/10.1007/s11356-021-17654-5.

Data availability All data generated or analyzed during this study are included in this published article (and its supplementary information files).

Declarations

Ethics approval and consent to participate Not applicable.

Consent for publication Not applicable.

Competing interests The authors declare no competing interests.

References

An D, Westerhoff P, Zheng M, Wu M, Yang Y, Chiu CA (2015) UV-activated persulfate oxidation and regeneration of NOM-saturated granular activated carbon. Water Res 73:304–310. https://doi.org/10.1016/j.watres.2015.01.040

Anfar Z, El Fakir AA, Zbair M, Hafidi Z, Amedlous A, Majdoub M, Farsad S, Amjlef A, Jada A, El Alem N (2021) New functionalization approach synthesis of sulfur doped, nitrogen doped and Co-doped porous carbon: superior metal-free carbocatalyst for the catalytic oxidation of aqueous organics pollutants. Chem Eng J 405:126660. https://doi.org/10.1016/j.cej.2020.126660

Azari A, Nabizadeh R, Nasseri S, Mahvi AH, Mesdaghinia AR (2020) Comprehensive systematic review and meta-analysis of dyes adsorption by carbon-based adsorbent materials: classification and analysis of last decade studies. Chemosphere 250:126238. https://doi.org/10.1016/j.chemosphere.2020.126238

Ceretta MB, Vieira Y, Wolski EA, Foletto EL, Silvestri S (2020) Biological degradation coupled to photocatalysis by ZnO/polypyrrole composite for the treatment of real textile wastewater. J Water Proc Eng 35:101230. https://doi.org/10.1016/j.jwpe.2020.101230

Chen L, Hu P, Zhang L, Huang S, Luo L, Huang C (2012) Toxicity of graphene oxide and multi-walled carbon nanotubes against human cells and zebrafish. Sci China Chem 55:2209–2216. https://doi.org/10.1007/s11426-012-4620-z

Chen S, Huang Y, Han X, Wu Z, Lai C, Wang J, Deng Q, Zeng Z, Deng S (2018) Simultaneous and efficient removal of Cr(VI) and methyl orange on LDHs decorated porous carbons. Chem Eng J 352:306–315. https://doi.org/10.1016/j.cej.2018.07.012

Chen Z, Wang J, Pu Z, Zhao Y, Jia D, Chen H, Wen T, Hu B, Alsaedi A, Hayat T, Wang X (2017) Synthesis of magnetic Fe$_3$O$_4$/CFA composites for the efficient removal of U(VI) from wastewater. Chem Eng J 320:448–457. https://doi.org/10.1016/j.cej.2017.03.074

Cheng G, Liu Y-L, Wang Z-G, Zhang J-L, Sun D-H, Ni J-Z (2012) The GO/rGO–Fe$_3$O$_4$ composites with good water-dispersibility and fast magnetic response for effective immobilization and enrichment of biomolecules. J Mater Chem 22:21998–22004. https://doi.org/10.1039/c2jm33695b

Cheng X, Li P, Zhu X, Luo C, Zheng L, Hou C, Wu D, Liang H (2021) Role of different dimensional carbon nanoparticles in catalytic oxidation of organic pollutants and alleviating membrane fouling during ultrafiltration of surface water. Sep Purif Technol 270:118804. https://doi.org/10.1016/j.seppur.2021.118804

Dai J, Xie A, Zhang R, Ge W, Chang Z, Tian S, Li C, Yan Y (2018) Scalable preparation of hierarchical porous carbon from lignin for highly efficient adsorptive removal of sulfamethazine antibiotic. J Mol Liq 256:203–212. https://doi.org/10.1016/j.molliq.2018.02.042

Deng Y, Ok YS, Mohan D, Pittman CU Jr, Dou X (2019) Carbamazepine removal from water by carbon dot-modified magnetic carbon nanotubes. Environ Res 169:434–444. https://doi.org/10.1016/j.envres.2018.11.035

Doan VD, Nguyen NV, Nguyen TL, Tran VA, Le VT (2021) High-efficient reduction of methylene blue and 4-nitrophenol by silver nanoparticles embedded in magnetic graphene oxide. Environ Sci Pollut R. https://doi.org/10.1007/s11356-021-13597-z

Doekhi-Bennani Y, Leilabady NM, Fu M, Rietveld LC, van der Hoek JP, Heijman SGJ (2021) Simultaneous removal of ammonium ions and sulfamethoxazole by ozone regenerated high silica zeolites. Water Res 188:116472. https://doi.org/10.1016/j.watres.2020.116472

E T, Ma D, Yang S, Hao X (2020) Graphene oxide-montmorillonite/sodium alginate aerogel beads for selective adsorption of methylene blue in wastewater. J Alloy Compd 832:154833. https://doi.org/10.1016/j.jallcom.2020.154833

Eltaweil AS, Elgarhy GS, El-Subruiti GM, Omer AM (2020) Carboxymethyl cellulose/carboxylated graphene oxide composite microbeads for efficient adsorption of cationic methylene blue dye. Int J Biol Macromol 154:307–318. https://doi.org/10.1016/j.ijbiomac.2020.03.122

Ersan G, Apul OG, Perreault F, Karanfil T (2017) Adsorption of organic contaminants by graphene nanosheets: a review. Water Res 126:385–398. https://doi.org/10.1016/j.watres.2017.08.010

Fan X, Lin H, Zhao J, Mao Y, Zhang J, Zhang H (2021) Activation of peroxymonosulfate by sewage sludge biochar-based catalyst for efficient removal of bisphenol A: performance and mechanism. Sep Purif Technol 272:118909. https://doi.org/10.1016/j.seppur.2021.118909

Fatima B, Siddiqui SI, Nirala RK, Vikrant K, Kim K-H, Ahmad R, Chaudhry SA (2020) Facile green synthesis of ZnO-CdWO$_4$ nanoparticles and their potential as adsorbents to remove organic dye. Environ Pollut 271:116401. https://doi.org/10.1016/j.envpol.2020.116401

Gamal ME, Mousa HA, El-Naas MH, Zacharia R, Judd S (2018) Bio-regeneration of activated carbon: a comprehensive review. Sep Purif Technol 197:345–359. https://doi.org/10.1016/j.seppur.2018.01.015

Gong X-B (2016) Degradation of dye wastewater by persulfate activated with Fe$_3$O$_4$/graphene nanocomposite. J Water Reuse Desal 6:553–561. https://doi.org/10.2166/wrd.2016.187

Gross KC, Seybold PG (2001) Substituent effects on the physical properties and pK$_a$ of phenol. Int J Quantum Chem 85:569–579. https://doi.org/10.1002/qua.1525

Guo Y, Yan L, Li X, Yan T, Song W, Hou T, Tong C, Mu J, Xu M (2021) Goethite/biochar-activated peroxymonosulfate enhances tetracycline degradation: inherent roles of radical and non-radical processes. Sci Total Environ 783:147102. https://doi.org/10.1016/j.scitotenv.2021.147102

Gupta K, Khatri OP (2017) Reduced graphene oxide as an effective adsorbent for removal of malachite green dye: plausible adsorption pathways. J Colloid Interf Sci 501:11–21. https://doi.org/10.1016/j.jcis.2017.04.035

Hajahmadi Z, Younesi H, Bahramifar N, Khakpour H, Pirzadeh K (2015) Multicomponent isotherm for biosorption of Zn(II), CO(II) and Cd(II) from ternary mixture onto pretreated dried Aspergillus niger biomass. Water Resour Ind 11:71–80. https://doi.org/10.1016/j.wri.2015.07.003

He Q, Wang G, Chen Z, Miao Z, Wan K, Huang S (2020) Adsorption of anionic azo dyes using lignite coke by one-step short-time pyrolysis. Fuel 267:117140. https://doi.org/10.1016/j.fuel.2020.117140

Hollingsworth CA, Seybold PG, Hadad CM (2002) Substituent effects on the electronic structure and pK$_a$ of benzoic acid. Int J Quantum Chem 90:1396–1403. https://doi.org/10.1002/qua.10362

Hu L, Huang Y, Chen Q (2013) Fe$_x$Co$_3$−xO$_4$ nanoporous particles stemmed from metal–organic frameworks Fe3[Co(CN)6]2: a highly efficient material for removal of organic dyes from water. J Alloy Compd 559:57–63. https://doi.org/10.1016/j.jallcom.2013.01.095

Huang Z, Li Z, Zheng L, Zhou L, Chai Z, Wang X, Shi W (2017) Interaction mechanism of uranium(VI) with three-dimensional graphene oxide-chitosan composite: insights from batch experiments, IR, XPS, and EXAFS spectroscopy. Chem Eng J 328:1066–1074. https://doi.org/10.1016/j.cej.2017.07.067

Hubbe MA (2021) Insisting upon meaningful results from adsorption experiments. Sep Purif Rev. https://doi.org/10.1080/15422119.2021.1888299

Hutson A, Ko S, Huling SG (2012) Persulfate oxidation regeneration of granular activated carbon: reversible impacts on sorption behavior. Chemosphere 89:1218–1223. https://doi.org/10.1016/j.chemosphere.2012.07.040

Ighalo JO, Iwuozor KO, Igwegbe CA, Adeniyi AG (2021) Verification of pore size effect on aqueous-phase adsorption kinetics: a case study of methylene blue. Colloid Surface A 626:127119. https://doi.org/10.1016/j.colsurfa.2021.127119

Ji Y, Xu F, Wei W, Gao H, Zhang K, Zhang G, Xu Y, Zhang P (2021) Efficient and fast adsorption of methylene blue dye onto a nanosheet MFI zeolite. J Solid State Chem 295:121917. https://doi.org/10.1016/j.jssc.2020.121917

Kah M, Sigmund G, Xiao F, Hofmann T (2017) Sorption of ionizable and ionic organic compounds to biochar, activated carbon and other carbonaceous materials. Water Res 124:673–692. https://doi.org/10.1016/j.watres.2017.07.070

Khan A, Wang J, Li J, Wang X, Chen Z, Alsaedi A, Hayat T, Chen Y, Wang X (2017) The role of graphene oxide and graphene oxide-based nanomaterials in the removal of pharmaceuticals from aqueous media: a review. Environ Sci Pollut R 24:7938–7958. https://doi.org/10.1007/s11356-017-8388-8

Khan A, Zhang K, Taraqqi-A-Kamal A, Xiaoguang W, Chen Y, Zhang Y (2021) Degradation of antibiotics in aqueous media using manganese nanocatalyst-activated peroxymonosulfate. J Colloid Interf Sci 599:805–818. https://doi.org/10.1016/j.jcis.2021.04.095

Khan FSA, Mubarak NM, Tan YH, Karri RR, Khalid M, Walvekar R, Abdullah EC, Mazari SA, Nizamuddin S (2020) Magnetic nano-particles incorporation into different substrates for dyes and heavy metals removal-a review. Environ Sci Pollut R 27:43526–43541. https://doi.org/10.1007/s11356-020-10482-z

Lee J, Sohn Y, Park JH, Lee S, Kim B-S, Park I-S, Kim P (2019) Preparation and electrochemical performance of titanium nitride-graphene nanocomposite with high Ti contents and tailored morphology. Curr Appl Phys 19:961–967. https://doi.org/10.1016/j.cap.2019.05.015

Li Q, Yue Q-Y, Su Y, Gao B-Y, Sun H-J (2010) Equilibrium, thermodynamics and process design to minimize adsorbent amount for the adsorption of acid dyes onto cationic polymer-loaded bentonite. Chem Eng J 158:489–497. https://doi.org/10.1016/j.cej.2010.01.033

Li R, Gao B, Guo K, Yue Q, Zheng H, Wang Y (2017) Effects of papermaking sludge-based polymer on coagulation behavior in the disperse and reactive dyes wastewater treatment. Bioresource Technol 240:59–67. https://doi.org/10.1016/j.biortech.2017.02.088

Liu C, Li C, Shan Y, Sun Z, Chen W (2020a) Comparison of two typical regeneration methods to the spent biological activated carbon in drinking water. Environ Sci Pollut Res Int 27:16404–16414. https://doi.org/10.1007/s11356-019-07440-9

Liu Z, Ren B, Ding H, He H, Deng H, Zhao C, Wang P, Dionysiou DD (2020b) Simultaneous regeneration of cathodic activated carbon fiber and mineralization of desorbed contaminations by electro-peroxydisulfate process: advantages and limitations. Water Res 171:115456. https://doi.org/10.1016/j.watres.2019.115456

Lu P-J, Lin H-C, Yu W-T, Chern J-M (2011) Chemical regeneration of activated carbon used for dye adsorption. J Taiwan Inst Chem E 42:305–311. https://doi.org/10.1016/j.jtice.2010.06.001

Mahdavi AR, Ghoresyhi AA, Rahimpour A, Younesi H, Pirzadeh K (2018) COD removal from landfill leachate using a high-performance and low-cost activated carbon synthesized from walnut shell. Chem Eng Commun 205:1193–1206. https://doi.org/10.1080/00986445.2018.1441831

McQuillan RV, Stevens GW, Mumford KA (2018) The electrochemical regeneration of granular activated carbons: a review. J Hazard Mater 355:34–49. https://doi.org/10.1016/j.jhazmat.2018.04.079

Missaoui K, Ouertani R, Jbira E, Boukherroub R, Bessais B (2021) Morphological influence of BiVO$_4$ nanostructures on peroxymonosulfate activation for highly efficient catalytic degradation of rhodamine B. Environ Sci Pollut Res Int. https://doi.org/10.1007/s11356-021-14320-8

Molaei MJ (2021) Magnetic graphene, synthesis, and applications: a review. Mater Sci Eng, B 272:115325. https://doi.org/10.1016/j.mseb.2021.115325

Muniyalakshmi M, Sethuraman K, Silambarasan D (2020) Synthesis and characterization of graphene oxide nanosheets. Materials Today: Proceedings 21:408–410. https://doi.org/10.1016/j.matpr.2019.06.375

Ovchinnikov OV, Evtukhova AV, Kondratenko TS, Smirnov MS, Khokhlov VY, Erina OV (2016) Manifestation of intermolecular interactions in FTIR spectra of methylene blue molecules. Vib Spectrosc 86:181–189. https://doi.org/10.1016/j.vibspec.2016.06.016

Partlan E, Ren Y, Apul OG, Ladner DA, Karanfil T (2020) Adsorption kinetics of synthetic organic contaminants onto superfine powdered activated carbon. Chemosphere 253:126628. https://doi.org/10.1016/j.chemosphere.2020.126628

Pirzadeh K, Ghoreyshi AA (2013) Phenol removal from aqueous phase by adsorption on activated carbon prepared from paper mill sludge. Desalin Water Treat 52:6505–6518. https://doi.org/10.1080/19443994.2013.821034

Pirzadeh K, Ghoreyshi AA, Rahimnejad M, Mohammadi M (2018) Electrochemical synthesis, characterization and application of a microstructure $Cu_3(BTC)_2$ metal organic framework for CO_2 and CH_4 separation. Korean J Chem Eng 35:974–983. https://doi.org/10.1007/s11814-017-0340-6

Qian F, Yin H, Liu F, Sheng J, Gao S, Shen Y (2021) The in situ catalytic oxidation of sulfamethoxazole via peroxydisufate activation operated in a NG/rGO/CNTs composite membrane filtration. Environ Sci Pollut R 28:26828–26839. https://doi.org/10.1007/s11356-021-12545-1

Rafatullah M, Sulaiman O, Hashim R, Ahmad A (2010) Adsorption of methylene blue on low-cost adsorbents: a review. J Hazard Mater 177:70–80. https://doi.org/10.1016/j.jhazmat.2009.12.047

Ramesha GK, Kumara AV, Muralidhara HB, Sampath S (2011) Graphene and graphene oxide as effective adsorbents toward anionic and cationic dyes. J Colloid Interface Sci 361:270–277. https://doi.org/10.1016/j.jcis.2011.05.050

Ramirez-Ubillus MA, de Melo C-S, Hammer P, Nogueira RFP (2021) A new approach on synergistic effect and chemical stability of graphene oxide-magnetic nanocomposite in the heterogeneous Fenton degradation of caffeine. Environ Sci Pollut Res Int. https://doi.org/10.1007/s11356-021-14714-8

Rani M, Shanker U (2021) Insight in to sunlight-driven rapid photocatalytic degradation of organic dyes by hexacyanoferrate-based nanoparticles. Environ Sci Pollut R 28:5637–5650. https://doi.org/10.1007/s11356-020-10925-7

Ren W, Xiong L, Nie G, Zhang H, Duan X, Wang S (2020) Insights into the electron-transfer regime of peroxydisulfate activation on carbon nanotubes: the role of oxygen functional groups. Environ Sci Technol 54:1267–1275. https://doi.org/10.1021/acs.est.9b06208

Sadrnia A, Orooji Y, Behmaneshfar A, Darabi R, Maghsoudlou Kamali D, Karimi-Maleh H, Opoku F, Govender PP (2021) Developing a simple box-behnken experimental design on the removal of doxorubicin anticancer drug using Fe_3O_4/graphene nanoribbons adsorbent. Environ Res 200:111522. https://doi.org/10.1016/j.envres.2021.111522

Schirmer RH, Adler H, Pickhardt M, Mandelkow E (2011) Lest we forget you–methylene blue. Neurobiol Aging 32:e2327–e2316. https://doi.org/10.1016/j.neurobiolaging.2010.12.012

Shi Y, Zhu J, Yuan G, Liu G, Wang Q, Sun W, Zhao B, Wang L, Zhang H (2020) Activation of persulfate by EDTA-2K-derived nitrogen-doped porous carbons for organic contaminant removal: radical and non-radical pathways. Chem Eng J 386:124009. https://doi.org/10.1016/j.cej.2019.124009

Simonin J-P (2016) On the comparison of pseudo-first order and pseudo-second order rate laws in the modeling of adsorption kinetics. Chem Eng J 300:254–263. https://doi.org/10.1016/j.cej.2016.04.079

Singh N, Riyajuddin S, Ghosh K, Mehta SK, Dan A (2019) Chitosan-graphene oxide hydrogels with embedded magnetic iron oxide nanoparticles for dye removal. ACS Applied Nano Materials 2:7379–7392. https://doi.org/10.1021/acsanm.9b01909

Solís RR, Dinc Ö, Fang G, Nadagouda MN, Dionysiou DD (2021) Activation of inorganic peroxides with magnetic graphene for the removal of antibiotics from wastewater. Environ Sci Nano 8:960–977. https://doi.org/10.1039/D0EN01280G

Solis RR, Mena IF, Nadagouda MN, Dionysiou DD (2020) Adsorptive interaction of peroxymonosulfate with graphene and catalytic assessment via non-radical pathway for the removal of aqueous pharmaceuticals. J Hazard Mater 384:121340. https://doi.org/10.1016/j.jhazmat.2019.121340

Song G, Li A, Shi Y, Li W, Wang H, Wang C, Li R, Ding G (2021) Sorptive removal of methylene blue from water by magnetic multi-walled carbon nanotube composites. Environ Sci Pollut Res Int. https://doi.org/10.1007/s11356-021-13543-z

Soni S, Bajpai PK, Mittal J, Arora C (2020) Utilisation of cobalt doped Iron based MOF for enhanced removal and recovery of methylene blue dye from waste water. J Mol Liq 314:113642. https://doi.org/10.1016/j.molliq.2020.113642

Tan KL, Hameed BH (2017) Insight into the adsorption kinetics models for the removal of contaminants from aqueous solutions. J Taiwan Inst Chem E 74:25–48. https://doi.org/10.1016/j.jtice.2017.01.024

Teli MD, Nadathur GT (2018) Adsorptive removal of acid yellow 17 (an anionic dye) from water by novel ionene chloride modified electrospun silica nanofibres. J Enviro Chem Eng 6:7257–7272. https://doi.org/10.1016/j.jece.2018.10.005

Tian W, Lin J, Zhang H, Duan X, Sun H, Wang H, Wang S (2020) Enhanced removals of micropollutants in binary organic systems by biomass derived porous carbon/peroxymonosulfate. J Hazard Mater: 124459. https://doi.org/10.1016/j.jhazmat.2020.124459

Tran HN, You SJ, Hosseini-Bandegharaei A, Chao HP (2017) Mistakes and inconsistencies regarding adsorption of contaminants from aqueous solutions: a critical review. Water Res 120:88–116. https://doi.org/10.1016/j.watres.2017.04.014

Wang J, Duan X, Dong Q, Meng F, Tan X, Liu S, Wang S (2019) Facile synthesis of N-doped 3D graphene aerogel and its excellent performance in catalytic degradation of antibiotic contaminants in water. Carbon 144:781–790. https://doi.org/10.1016/j.carbon.2019.01.003

Wang S, Gao S, Tian J, Wang Q, Wang T, Hao X, Cui F (2020a) A stable and easily prepared copper oxide catalyst for degradation of organic pollutants by peroxymonosulfate activation. J Hazard Mater 387:121995. https://doi.org/10.1016/j.jhazmat.2019.121995

Wang W, Cao Y, Hu X, Zhou S, Zhu D, Qi D, Deng S (2020b) Granular reduced graphene oxide/Fe_3O_4 hydrogel for efficient adsorption and catalytic oxidation of p-perfluorous nonenoxybenzene sulfonate. J Hazard Mater 386:121662. https://doi.org/10.1016/j.jhazmat.2019.121662

Wang Y, Lin C, Liu X, Ren W, Huang X, He M, Ouyang W (2021) Efficient removal of acetochlor pesticide from water using magnetic activated carbon: adsorption performance, mechanism, and regeneration exploration. Sci Total Environ 778:146353. https://doi.org/10.1016/j.scitotenv.2021.146353

Yang S-T, Chen S, Chang Y, Cao A, Liu Y, Wang H (2011) Removal of methylene blue from aqueous solution by graphene oxide. J Colloid Interf Sci 359:24–29. https://doi.org/10.1016/j.jcis.2011.02.064

Yang S, Xu S, Tong J, Ding D, Wang G, Chen R, Jin P, Wang XC (2021) Overlooked role of nitrogen dopant in carbon catalysts for peroxymonosulfate activation: intrinsic defects or extrinsic defects? Appl Catal B Environ 295:120291. https://doi.org/10.1016/j.apcatb.2021.120291

Yang X, Chen C, Li J, Zhao G, Ren X, Wang X (2012) Graphene oxide-iron oxide and reduced graphene oxide-iron oxide hybrid materials for the removal of organic and inorganic pollutants. RSC Adv 2:8821–8826. https://doi.org/10.1039/c2ra20885g

Yao G, Liu X, Zhang G, Han Z, Liu H (2021) Green synthesis of tannic acid functionalized graphene hydrogel to efficiently adsorb methylene blue. Colloid Surface A 625:126972. https://doi.org/10.1016/j.colsurfa.2021.126972

Yin F, Wang C, Lin K-YA, Tong S (2019) Persulfate activation for efficient degradation of norfloxacin by a rGO-Fe$_3$O$_4$ composite. J Taiwan Inst Chem E 102:163–169. https://doi.org/10.1016/j.jtice.2019.05.022

Zhang X, Li A, Jiang Z, Zhang Q (2006) Adsorption of dyes and phenol from water on resin adsorbents: effect of adsorbate size and pore size distribution. J Hazard Mater 137:1115–1122. https://doi.org/10.1016/j.jhazmat.2006.03.061

Zhang Y, Liu L, Zhang P, Wang J, Xu M, Deng Q, Zeng Z, Deng S (2019) Ultra-high surface area and nitrogen-rich porous carbons prepared by a low-temperature activation method with superior gas selective adsorption and outstanding supercapacitance performance. Chem Eng J 355:309–319. https://doi.org/10.1016/j.cej.2018.08.169

Zhang Y, Zhao H, Wen J, Ding S, Wang W (2021) Insights into the nonradical degradation mechanisms of antibiotics in persulfate activation by tourmaline. Sep Purif Technol 270:118772. https://doi.org/10.1016/j.seppur.2021.118772

Zhao B, Long X, Wang H, Wang L, Qian Y, Zhang H, Yang C, Zhang Z, Li J, Ma C, Shi Y (2021) Polyamide thin film nanocomposite membrane containing polydopamine modified ZIF-8 for nanofiltration. Colloid Surface A 612:125971. https://doi.org/10.1016/j.colsurfa.2020.125971

Zhou W, Meng X, Gao J, Zhao H, Zhao G, Ma J (2020a) Electrochemical regeneration of carbon-based adsorbents: a review of regeneration mechanisms, reactors, and future prospects. Chem Eng J Adv 5:100083. https://doi.org/10.1016/j.ceja.2020.100083

Zhou X, Zhao Q, Wang J, Chen Z, Chen Z (2020b) Nonradical oxidation processes in PMS-based heterogeneous catalytic system: generation, identification, oxidation characteristics, challenges response and application prospects. Chem Eng J 410:128312. https://doi.org/10.1016/j.cej.2020.128312

Zhu W, Jiang X, Liu F, You F, Yao C (2020) Preparation of chitosan-graphene oxide composite aerogel by hydrothermal method and its adsorption property of methyl orange. Polymers 12:2169. https://doi.org/10.3390/polym12092169

Zhu Y, Huang H, Zhou W, Li G, Liang X, Guo J, Tang S (2017) Low temperature reduction of graphene oxide film by ammonia solution and its application for high-performance supercapacitors. J Mater Sci Mater El 28:10098–10105. https://doi.org/10.1007/s10854-017-6771-3